JOURNAL OF SYNCHROTRON RADIATION

ISSN 1600-5775

Quantifying redox heterogeneity in single-crystalline $LiCoO_2$ cathode particles

Chenxi Wei,[a,b]‡ Yanshuai Hong,[c]‡ Yangchao Tian,[a]* Xiqian Yu,[c]* Yijin Liu[b]* and Piero Pianetta[b]

[a]National Synchrotron Radiation Laboratory, University of Science and Technology of China, Hefei, Anhui 230027, People's Republic of China, [b]Stanford Synchrotron Radiation Lightsource, SLAC National Accelerator Laboratory, Menlo Park, CA 94025, USA, and [c]Beijing Advanced Innovation Center for Materials Genome Engineering, Institute of Physics, Chinese Academy of Sciences, Beijing 100190, People's Republic of China.
*Correspondence e-mail: ychtian@ustc.edu.cn, xyu@iphy.ac.cn, liuyijin@slac.stanford.edu

Received 20 October 2019
Accepted 13 February 2020

Edited by A. F. Craievich, University of São Paulo, Brazil

‡ These authors contributed equally to this work

Keywords: spectro-microscopy; X-ray polarization; single-crystalline $LiCoO_2$.

Supporting information: this article has supporting information at journals.iucr.org/s

Active cathode particles are fundamental architectural units for the composite electrode of Li-ion batteries. The microstructure of the particles has a profound impact on their behavior and, consequently, on the cell-level electrochemical performance. $LiCoO_2$ (LCO, a dominant cathode material) is often in the form of well-shaped particles, a few micrometres in size, with good crystallinity. In contrast to secondary particles (an agglomeration of many fine primary grains), which are the other common form of battery particles populated with structural and chemical defects, it is often anticipated that good particle crystallinity leads to superior mechanical robustness and suppressed charge heterogeneity. Yet, sub-particle level charge inhomogeneity in LCO particles has been widely reported in the literature, posing a frontier challenge in this field. Herein, this topic is revisited and it is demonstrated that X-ray absorption spectra on single-crystalline particles with highly anisotropic lattice structures are sensitive to the polarization configuration of the incident X-rays, causing some degree of ambiguity in analyzing the local spectroscopic fingerprint. To tackle this issue, a methodology is developed that extracts the white-line peak energy in the X-ray absorption near-edge structure spectra as a key data attribute for representing the local state of charge in the LCO crystal. This method demonstrates significantly improved accuracy and reveals the mesoscale chemical complexity in LCO particles with better fidelity. In addition to the implications on the importance of particle engineering for LCO cathodes, the method developed herein also has significant impact on spectro-microscopic studies of single-crystalline materials at synchrotron facilities, which is broadly applicable to a wide range of scientific disciplines well beyond battery research.

1. Introduction

The rapidly increasing demand for portable electronics and electrical vehicles has brought energy-storage technology to the focal point of the tremendous ongoing research effort across the globe. In the current landscape of this field, Li-ion batteries (LIBs) are the most popular and promising energy-storage devices. LIBs are made of two electrodes (the anode and the cathode) that consecutively host and release charge carriers (*i.e.* electrons and lithium ions) as the system is electrochemically cycled. It has been revealed that the structural and chemical complexity in this system exist across a wide range of length scales, ranging from the atomic level to the device level, highlighting the importance of probing the interplay among lattice, charge and morphology of the electrode materials.

A suite of synchrotron-based X-ray tools (Lin *et al.*, 2017; Bak *et al.*, 2018; Cao, Toney *et al.*, 2019; Heenan *et al.*, 2019;

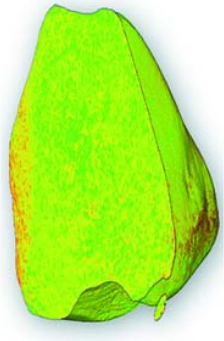

Nelson Weker & Toney, 2015) have been utilized to study the electrode materials' behaviors upon battery operation. These examples include but are not limited to using X-ray diffraction to investigate the active materials' lattice structural evolution (Zhu *et al.*, 2018), using hard X-ray absorption spectroscopy (hard XAS) to probe the valence state of the transition-metal elements in the bulk of the electrode (Aquilanti *et al.*, 2017), using soft X-ray absorption spectroscopy (soft XAS) over the *L* edges of the transition-metal elements to investigate the surface-damage effect (Lin *et al.*, 2014), using soft X-ray resonant inelastic X-ray scattering to probe the oxygen's redox activity in the cathode materials in deeply delithiated state (Gent *et al.*, 2017; Dai *et al.*, 2019; Li, Lee *et al.*, 2019; Xu, Sun *et al.*, 2018), using X-ray reflectivity measurements to understand the solid electrolyte interphase (Cao *et al.*, 2016; Steinrück *et al.*, 2018; Cao, Abate *et al.*, 2019), and using X-ray microscopy to reconstruct the morphological degradation (Yang *et al.*, 2019; Xia *et al.*, 2018; Besli, Xia *et al.*, 2019; Mao *et al.*, 2019) and lattice defect evolution (Singer *et al.*, 2018) in the battery electrode.

In addition to the above-mentioned efforts, there is a growing interest in understanding the thermal-electro-chemo-mechanical interplay within individual battery particles [*i.e.* at the mesoscale (Wei, Xia *et al.*, 2018)]. X-ray spectro-microscopy has been regarded as a powerful tool for such study as it could spatially resolve the local chemistry by extracting the spectroscopic fingerprints associated with every volume unit (*i.e.* voxels at tens of nanometres) (Meirer *et al.*, 2011). Successful applications of this technique can be found in studies of many different cathode materials including many of those that play major roles in today's market, like $LiCoO_2$ (LCO; Xu *et al.*, 2017; Zhang *et al.*, 2017), $LiFePO_4$ (Boesenberg *et al.*, 2013; Wang *et al.*, 2016; Hong *et al.*, 2017) and $LiNi_xMn_yCo_{(1-x-y)}O_2$ (Lin *et al.*, 2016; Gent *et al.*, 2016). Meanwhile, *in situ/operando* spectro X-ray imaging experiments are also carried out to elucidate the cathode materials' response to different reaction driving forces (Xu *et al.*, 2017; Nelson Weker *et al.*, 2017), highlighting the structural and chemical complexity under non-equilibrium conditions. Through these systematic efforts, researchers in this field are putting together, piece by piece, a more comprehensive understanding of the relationship among the sub-particle level morphology defects and damages, state-of-charge (SoC) heterogeneity, and the cell-level electrochemical performance.

In a typical full-field spectro-microscopic experiment, it is vital to efficiently analyze the spectra with a good degree of automation. This is because the spectra are effectively recorded at a data rate of ∼6000 Hz (2000 × 2000 pixel spectra in ∼10 minutes). There are many critical spectroscopic features in a XAS spectrum, *e.g.* the edge energy, peak energy, pre-edge and the first derivative of the X-ray absorption near-edge structure (XANES) spectra. In our case, the XANES spectra from a spectro-microscopic scan are extracted by tracking the intensity variation of each 30 nm pixel as a function of the incident energy. Moreover, because of its time-consuming nature (a 3D XANES scan takes ∼8–10 h to take tomograms at ∼60 energies of only one particle), the signal-to-noise ratio and the energy resolution of 3D XANES imaging data is not as good as those of a conventional bulk-averaged XAS scan. Because of these practical experimental constrains, it is not feasible to utilize the first derivative of the XANES spectra or the pre-edge signal for quantifying the XANES imaging data. The edge energy (the energy level that corresponds to the normalized intensity at 0.5) has been broadly utilized as a key data attribute for a rapid evaluation of the relative local oxidation state. In general, at the absorption *K*-edge of the transition-metal elements, the spectra shift along the axis of excitation energy as the valence state is changed. However, here we report that one of the key characteristics of the synchrotron source, the polarization of the X-ray illumination, has been overlooked in the previous studies. Omitting the polarization-dependent nature of the synchrotron spectro-imaging data could lead to unsatisfactory accuracy when investigating single-crystalline particles with highly anisotropic lattice structure, *e.g.* layered structure, in which the *c*-axis lattice parameter is much larger than that of the *a* and *b* axes (see Fig. S1 in the supporting information for comparison of a layered structure and a rock salt structure) (Kan *et al.*, 2018). Depending on the relative spatial arrangement of the *c* axis and the X-rays' major polarization axis, the spectroscopic fingerprints could be different for the crystals with exactly the same chemical state. A more robust approach that could better handle such a scenario is urgently needed as we are witnessing a rapidly growing interest in this research direction.

In this work, using LCO single-crystalline particles as a model system, we systematically tackled the above-discussed challenge and conducted the extraction of the local charge heterogeneity by analyzing the peak energy in the Co *K*-edge spectra, whose dependence on the polarization effect is significantly suppressed. By comparing LCO particles recovered from cells at different states of charge, we confirm that our development offers significantly improved accuracy in determining the local chemical state in comparison with the conventional approach that relies on the extraction of the edge energy. With this new approach, we take a closer look at a larger LCO particle which has been severely damaged by the electrochemical cycling. Our observation suggests that the particle-level structural and chemical defects could co-exist, highlighting the intertwined chemomechanical interplay at the mesoscale. Going beyond the study of LCO cathode materials, our development also offers profound impact on the spectro-microscopic investigation of single-crystalline materials using synchrotron facilities, where the X-rays have excellent properties (*e.g.* polarization and coherence) that need to be taken into consideration for proper interpretation of the experimental results.

2. Experimental section

2.1. Material synthesis

$LiCoO_2$ was synthesized by a solid-state reaction technique. Li_2CO_3 and Co_2O_3 were mixed in the stoichiometric ratio and grinded in an agate mortar for ∼30–40 min. Then the obtained

powders were made into pellets. The aim of the pellets, by making the reacting atoms closer to each other, was to increase crystallization. Finally, the pellets were calcinated at 900°C for 10 to 12 h in an air atmosphere using a box furnace. When sufficient temperature is reached, Li_2CO_3 and Co_2O_3 react via the following equation: $Li_2CO_3 + Co_2O_3 = 2LiCoO_2 + CO_2$.

2.2. Nano-resolution X-ray spectro-microscopy

X-ray spectroscopic imaging of the LCO particles was carried out using the transmission X-ray microscope installed at beamline 6-2c at the SSRL of the SLAC National Accelerator Laboratory. The nominal spatial resolution is ~30 nm. During the collection, powder samples are loaded into a quartz capillary, which is 100 µm in diameter and 10 µm in wall thickness. The capillary is mounted on the sample holder and is kept perpendicular to the incident X-ray beam (see Fig. S6 for a photograph of the sample holder with the mounted quartz capillary). Images at over 60 energy points were collected. The energy step away from the peak energy was set to 15 eV to ensure coverage of a relatively large window to carry out normalization, while the energy near peak energy was set to 1 eV to guarantee sufficient energy resolution. Data processing and analysis were performed using an in-house developed software known as *TXM-Wizard*. Details about the experimental configuration and the concept of the transmission X-ray microscopy (TXM)-based spectroscopic imaging method can be found elsewhere.

3. Results and discussion

3.1. Polarization-dependent spectroscopic signature of LCO crystal

In synchrotron-based X-ray spectro-microscopy, the transmission images of the sample are acquired as the incident X-ray energy is scanned across the absorption edge of an element of interest (Co in this present study). The absorption contrast of the sample changes as a function of the incident energy, yielding a spectroscopic signature that is often associated with the chemical state of the material. Tomographic scans are routinely adapted for resolving the structural and chemical heterogeneity along the beam path. A 3D XANES experiment can be carried out by performing tomography as a function of the energy or by conducting 2D spectro-microscopy in many different viewing angles (Liu *et al.*, 2012).

As illustrated in Fig. 1, in a 3D XANES dataset on a pristine single-crystalline LCO particle, we observed that the averaged XANES spectrum over the entire particle changes significantly as the particle is rotated along a vertical axis [see Figs. 1(*c*) to 1(*f*) for the averaged spectra at angles of −45°, 0°, 45° and 89°, and see Fig. S2 for the edge-energy maps at different viewing angles]. This particle was not subjected to

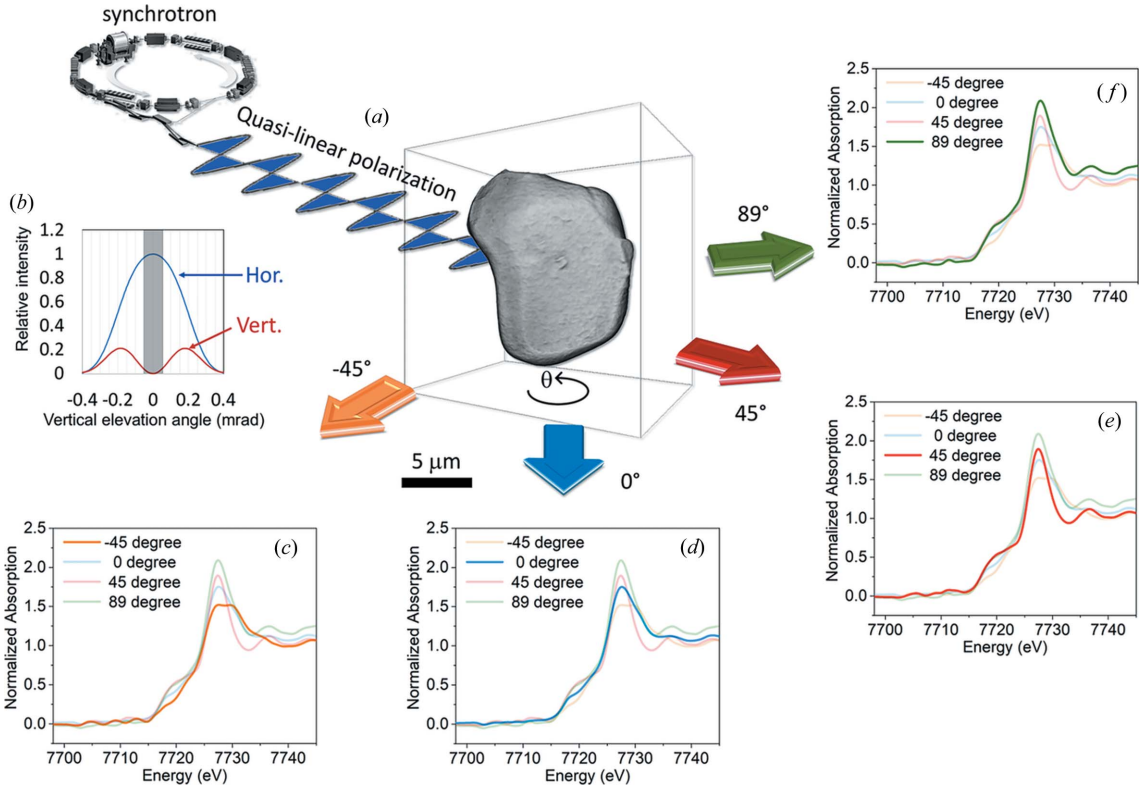

Figure 1
Illustration of the angular-dependent spectroscopic fingerprint of a pristine single-crystalline LCO particle. Panel (*a*) shows schematically the experimental configuration, where the particle is rotated along the vertical axis to facilitate the acquisition of the X-ray absorption spectra in different viewing angles [panels (*c*) to (*f*)]. Panel (*b*) shows the relative intensity profile of the horizontal and vertical polarization components as a function of the vertical elevation angle with respect to the X-ray source point that is ~30 m upstream of the sample. The scale bar in panel (*a*) is 5 µm.

any reaction active conditions; the differences in the averaged spectra are therefore attributed to the difference in the experimental configurations, *i.e.* the viewing angles, which brings our attention to the polarization effect.

This measurement was conducted at beamline 6-2c of the Stanford Synchrotron Radiation Lightsource (SSRL), where a 56-pole wiggler source generates a quasi-polarized illumination for illuminating the transmission X-ray microscope (Liu *et al.*, 2011). As confirmed by the relative intensity profiles of the horizontal and vertical polarization components, which changes as a function of the vertical elevation angle [see Fig. 1(*b*)], the horizontal polarization component is significantly stronger than the vertical component. Considering that the particle is only a few micrometres in diameter and is positioned at a distance of ∼30 m from the wiggler source, the measurement is effectively operated within the gray area in Fig. 1(*b*) and the particle practically sees X-rays that are linearly polarized in the horizontal direction (see Fig. S3 for more details about the polarization profile of the X-rays from SSRL). The lattice structure of $LiCoO_2$ crystal is highly anisotropic with its *c*-axis lattice parameter much larger than that of the *a* and *b* axes (see Fig. S1). Therefore, the relative spatial arrangement of the lattice *c* axis and the major polarization axis would have a significant impact on the spectroscopic signature, complicating the interpretation of the data.

3.2. Peak energy as a key descriptor for the SoC in LCO crystal

The polarization effect is usually overlooked in conventional battery research at synchrotron facilities because the battery electrodes are made of many particles with random lattice orientations. This is also the case for the study of secondary battery particles, which consist of a large number of primary grains with random orientations. The polarization effect would have been smeared out in those scenarios and is not detectable in the X-ray spectroscopic measurements. However, when dealing with single-crystalline particles this becomes an issue that needs to be carefully addressed. We show in Fig. 2(*a*) (and Fig. S4) the averaged XANES spectra over a single-crystalline LCO particle at different viewing angles. As highlighted in the magnified views, the edge energy, which has been broadly utilized as a proxy for the relative valence state, clearly shows an angular dependence. Such uncertainty makes the edge energy unfit for quantifying the valence state in the study of single-crystalline particles that have highly anisotropic lattice structures. On the other hand, the excitation energy of the first white-line peak [referred to as peak energy in this work, shown in the magnified views in the upper left of Figs. 2(*a*) and S5 for better comparison] appears to be relatively independent from the viewing angles, although the polarization effect results in a broadening of the white line and a splitting of the single-peak white line into a dual-peak structure at some viewing angles. For a better evaluation of this effect, we show in Fig. 2(*b*) the extracted edge energy, which appears to be a sine curve with the absolute value spread over a range of ∼3.1 eV. The peak energy, on the other hand, remains more or less constant (see also Fig. S5), considering that the instrumental energy resolution is ∼1 eV in our experiment. We further reconstructed the 3D distributions of the edge energy [Fig. 2(*c*)] and the peak energy [Fig. 2(*d*)] of the studied LCO particle. The color contrast shown in Fig. 2(*c*) is a result of the polarization effect, which would be interpreted as the local SoC heterogeneity if such a polarization effect is overlooked. The 3D peak-energy map in Fig. 2(*d*), on the other hand, appears to be relatively homogeneous, which makes sense because this LCO particle is in its pristine state.

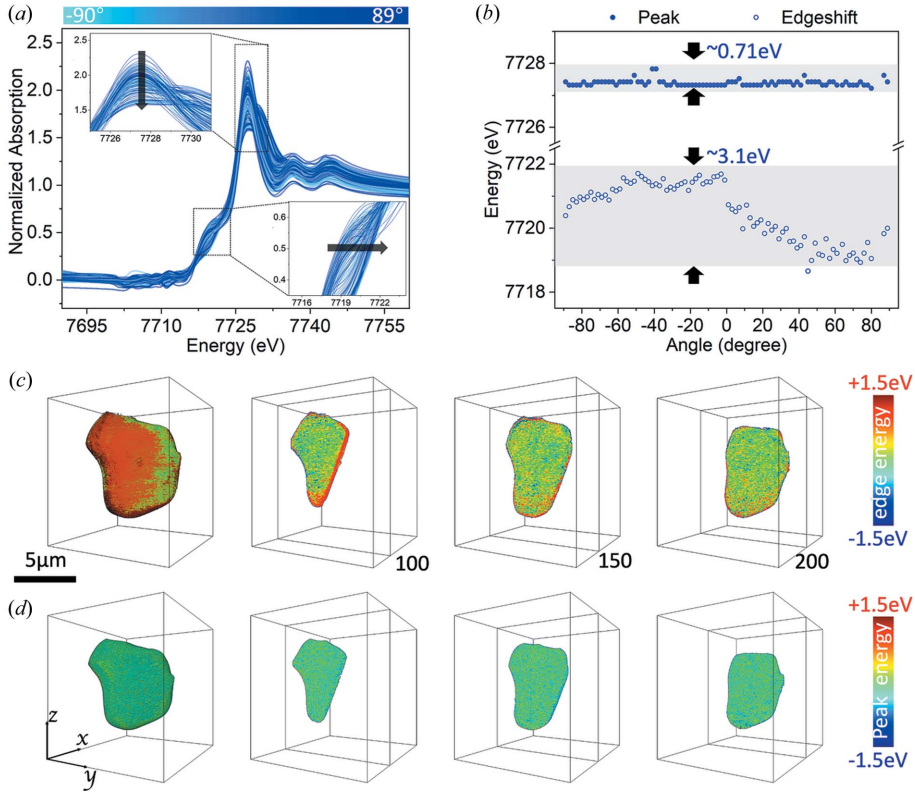

Figure 2
Comparison of the edge energy and peak energy as descriptors for quantifying the SoC of a single-crystalline LCO particle. Panel (*a*) shows the XANES spectra averaged over the entire particle at different viewing angles in a tomographic scan. Panel (*b*) is the extracted edge-energy and peak-energy values at different viewing angles. Panels (*c*) and (*d*) are the spatial distribution of edge energy and peak energy, respectively, recovered from a 3D XANES dataset on a single-crystalline LCO particle. In panels (*c*) and (*d*), the left column is the 3D rendering and the second to fourth columns are virtual slices through different depths of the particle.

3.3. Peak-energy map over a charged LCO particle

In the charged state, the cathode material often exhibits complicated properties that are relevant to the overall battery performance. For example, the formation of morphology defects (Xia *et al.*, 2018), the buildup of charge heterogeneity (Mao *et al.*, 2019) and the reduction in thermal stability (Wei, Zhang *et al.*, 2018; Mu *et al.*, 2018; Xu, Rahman *et al.*, 2018; Yan *et al.*, 2018; Besli, Shukla *et al.*, 2019) are all found in the cathode materials at deeply delithiated states. Therefore, we conducted 3D XANES analysis on a charged LCO particle using the method developed herein. We extracted the averaged XANES spectra at different viewing angles and compared the data from the pristine and charged particles in Fig. 3(*a*) (see the inset for the charging capacity–voltage curve). We clearly observed a shift of the white-line peak towards higher energy (by ∼0.7 eV) upon battery charging. For a more quantitative comparison between the edge energy and peak energy, we extracted these two values from the data and plotted them as a function of the viewing angle [Fig. 3(*b*)]. The peak energy of the charged particle (CD) is clearly separated from that of the pristine particle (P) regardless of the viewing angle, while the edge-energy curves are intertwined with each other. We therefore conclude that the peak energy is a more reliable data attribute for evaluating the Co's valence state in single-crystalline LCO particles. By using the peak energy as the key descriptor, the ambiguity caused by the polarization effect is minimized.

For a more comprehensive comparison between the charged and the pristine LCO particle, we show the virtual slices of spectro-tomographic data in Figs. 4(*a*) and 4(*b*), which represent the 3D peak-energy maps of the respective particles. The pristine particle appears to be homogeneous, while the charged particle shows some degree of redox heterogeneity in the bulk. The averaged Co *K*-edge XANES spectra over the entire particles are shown in Fig. 4(*c*) and the result is consistent with the angle-dependence analysis shown in Fig. 3. In addition to the change in the averaged oxidation state, the charged particle also exhibits a wider distribution of Co valence state as shown by the increased width in the probability distribution in Fig. 4(*d*).

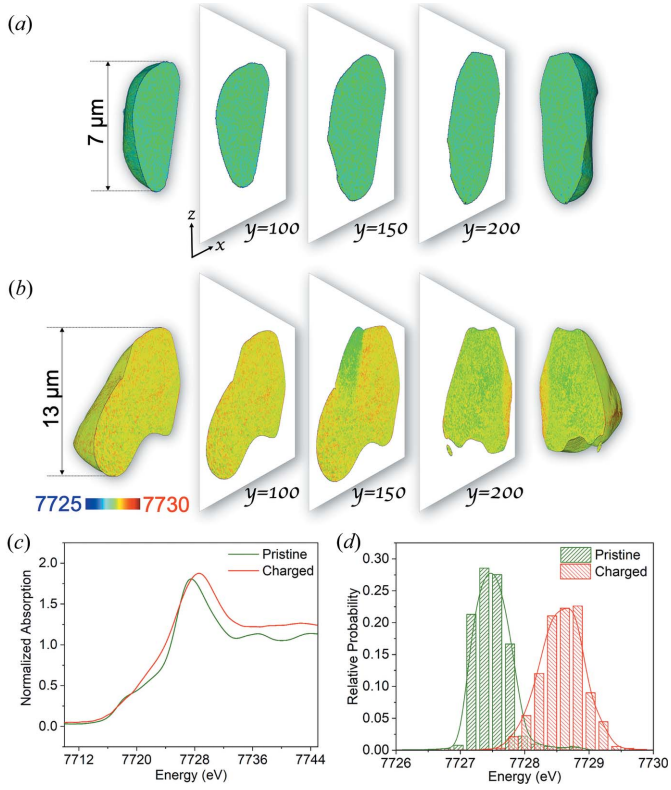

Figure 4
3D chemical mapping of the LCO particles in pristine and charged states using peak energy as the descriptor. Panels (*a*) and (*b*) show the chemical distribution of the pristine and charged LCO particles. Panel (*c*) is the representative multi-pixel averaged Co *K*-edge XANES spectra based on 3D XANES peak-energy maps. Panel (*d*) is the histogram of the peak energy's distribution.

3.4. Structural and chemical defects in severely damaged LCO particles

The above-discussed particles (presented in Fig. 4) are both single-crystalline particles with well-intact mesoscale structures. It is, however, anticipated that morphological and chemical defects will develop when the cathode material undergoes repeated cycling to high cut-off voltages. In deeply delithiated states, the lattice distortion (Singer *et al.*, 2018; Wang *et al.*, 2018; Li, Li *et al.*, 2019) could be severe and the anion redox (Zhang *et al.*, 2019; Gent *et al.*, 2017; Dai *et al.*, 2019; Li, Lee *et al.*, 2019; Xu, Sun *et al.*, 2018) could be activated. Such phenomena could be nucleation points for the accumulation of the mechanical strain that is eventually released through mesoscale particle cracking (Zhao *et al.*, 2019; Yan *et al.*, 2017; Tsai *et al.*, 2019; Markevich *et al.*, 2019). The formation of morphological defects (*e.g.* cracks) could in turn affect the local chemistry by exposing fresh solid interface to the liquid electrolyte and, subsequently,

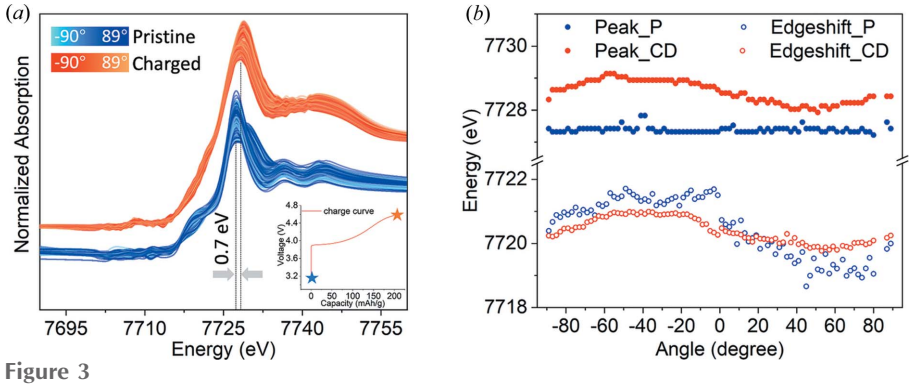

Figure 3
Comparison of the LCO particles in pristine and charged states to show the accuracy of the peak energy compared with edge energy. Panel (*a*) shows the comparison of the XANES spectra in different viewing angles from the pristine and charged particles. Panel (*b*) is the extracted edge energy and peak energy from the data at all viewing angles in the tomographic scan.

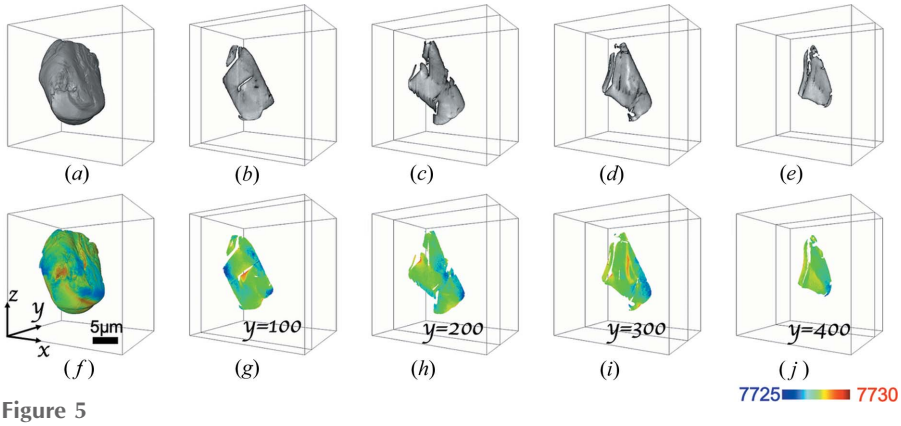

Figure 5
3D rendering of a charged LCO particle with complicated morphology. Panel (*a*) shows the 3D rendering of the particle morphology. Panels (*b*) to (*e*) are the slices in different depths of the *y* axis. Panels (*f*) to (*j*) are the corresponding 3D rendering peak-energy map and the peak-energy maps at different depths.

affecting the optimal diffusion pathways of the lithium ions and electrons.

Therefore, we choose to visualize a charged particle that appears to be more severely damaged (Fig. 5). As illustrated in Figs. 5(*a*)–5(*e*) (the 3D rendering of the morphology of the particle and several virtual slices through different depths), this particle is populated with cracks and domain boundaries. This severely damaged particle coexists with normal intact particles in the same electrode (they are recovered from the same electrode for the tomographic measurement), highlighting the electrode-level reaction heterogeneity. Although the whole cell is charged to a certain targeted cut-off voltage, local over-charge and over-discharge could coexist owing to the intrinsic complexity in the composite electrode, which could cause charge heterogeneity in the depth direction (cell polarization) (Xu *et al.*, 2019) and lateral directions (Yang *et al.*, 2019). The corresponding 3D peak-energy map over the same particle is shown in Figs. 5(*f*)–5(*j*), illustrating the morphology defect-induced local chemical complexity. The mesoscale charge heterogeneity in this particle could be caused by reaction inactive domain boundaries and cracks. Our observation clearly highlights the importance of surface and interface engineering, which could potentially be achieved through synthesis strategies, like doping and/or coating (Zhang *et al.*, 2019), and can be broadly applied regardless of the crystallinity of the starting material.

4. Conclusions

Visualizing and understanding battery-electrode particles could potentially offer valuable insight for the design of the next-generation battery materials. While synchrotron X-ray spectro-microscopy has been demonstrated as a powerful tool to investigate the local chemistry in battery particles, we highlight in this work that the X-ray polarization configuration could affect the data and the interpretation for single-crystalline materials with highly anisotropic lattice structures. Specific to the LCO particles, we revisited this problem and developed a new method to quantify the local valence state. By extracting the peak energy instead of edge energy as the key descriptor, we demonstrated that the undesired artifact caused by polarization is suppressed. We compared a charged LCO particle with a pristine one and demonstrated the accuracy and reliability of the proposed method. Finally, we studied a charged LCO particle with severe morphological damage. We visualized the coexisting morphological and chemical damage in the particle with improved fidelity and suggested that the surface modification could be effective in suppressing the unwanted charge heterogeneity. The method developed herein not only offers valuable implications on particle engineering for LCO cathode materials but also has significant impact on the spectro-microscopic study of single-crystal materials at synchrotron facilities, which is broadly applicable to a wide range of scientific disciplines well beyond battery research.

Acknowledgements

The engineering support from D. Van Campen, D. Day and V. Borzenets for the TXM experiment at beamline 6-2c of SSRL is gratefully acknowledged. YL and XY conceived this study. CW and YH participated in performing experiments and data processing. YT and PP contributed to the interpretation of the data. CW, YH, XY and YL wrote the manuscript with valuable input from all the co-authors. The authors declare no conflicts of interest.

Funding information

This work at the University of Science and Technology of China (USTC) was supported by the National Key R&D Program of China (grant No. 2017YFA0402904). Use of the SSRL, SLAC National Accelerator Laboratory, is supported by the US Department of Energy, Office of Science, Office of Basic Energy Sciences under Contract No. DE-AC02-76SF00515. The work carried out at the Institute of Physics (IOP), Chinese Academy of Sciences was supported by funding from the National Key R&D Program of China (grant No. 2016YFB0100100), the National Natural Science Foundation of China (grant Nos 51822211 and 11574281) and the Foundation for Innovative Research Groups of the National Natural Science Foundation of China (grant No. 51421002).

References

Aquilanti, G., Giorgetti, M., Dominko, R., Stievano, L., Arčon, I., Novello, N. & Olivi, L. (2017). *J. Phys. D Appl. Phys.* **50**, 074001.
Bak, S.-M., Shadike, Z., Lin, R., Yu, X. & Yang, X.-Q. (2018). *NPG Asia Mater.* **10**, 563–580.
Besli, M. M., Shukla, A. K., Wei, C., Metzger, M., Alvarado, J., Boell, J., Nordlund, D., Schneider, G., Hellstrom, S., Johnston, C., Christensen, J., Doeff, M. M., Liu, Y. & Kuppan, S. (2019). *J. Mater. Chem. A*, **7**, 12593–12603.

Besli, M. M., Xia, S., Kuppan, S., Huang, Y., Metzger, M., Shukla, A. K., Schneider, G., Hellstrom, S., Christensen, J., Doeff, M. M. & Liu, Y. (2019). *Chem. Mater.* **31**, 491–501.
Boesenberg, U., Meirer, F., Liu, Y., Shukla, A. K., Dell'Anna, R., Tyliszczak, T., Chen, G., Andrews, J. C., Richardson, T. J., Kostecki, R. & Cabana, J. (2013). *Chem. Mater.* **25**, 1664–1672.
Cao, C., Abate, I. I., Sivonxay, E., Shyam, B., Jia, C., Moritz, B., Devereaux, T. P., Persson, K. A., Steinrück, H.-G. & Toney, M. F. (2019). *Joule*, **3**, 762–781.
Cao, C., Steinrück, H.-G., Shyam, B., Stone, K. H. & Toney, M. F. (2016). *Nano Lett.* **16**, 7394–7401.
Cao, C., Toney, M. F., Sham, T.-K., Harder, R., Shearing, P. R., Xiao, X. & Wang, J. (2019). *Mater. Today*, doi:10.1016/j.mattod.2019.08.011.
Dai, K., Wu, J., Zhuo, Z., Li, Q., Sallis, S., Mao, J., Ai, G., Sun, C., Li, Z., Gent, W. E., Chueh, W. C., Chuang, Y., Zeng, R., Shen, Z., Pan, F., Yan, S., Piper, L. F. J., Hussain, Z., Liu, G. & Yang, W. (2019). *Joule*, **3**, 518–541.
Gent, W. E., Li, Y., Ahn, S., Lim, J., Liu, Y., Wise, A. M., Gopal, C. B., Mueller, D. N., Davis, R., Weker, J. N., Park, J.-H., Doo, S.-K. & Chueh, W. C. (2016). *Adv. Mater.* **28**, 6631–6638.
Gent, W. E., Lim, K., Liang, Y., Li, Q., Barnes, T., Ahn, S.-J., Stone, K. H., McIntire, M., Hong, J., Song, J. H., Li, Y., Mehta, A., Ermon, S., Tyliszczak, T., Kilcoyne, D., Vine, D., Park, J.-H., Doo, S.-K., Toney, M. F., Yang, W., Prendergast, D. & Chueh, W. C. (2017). *Nat. Commun.* **8**, 2091.
Heenan, T. M. M., Tan, C., Hack, J., Brett, D. J. L. & Shearing, P. R. (2019). *Mater. Today*, **31**, 69–85.
Hong, L., Li, L., Chen-Wiegart, Y.-K., Wang, J., Xiang, K., Gan, L., Li, W., Meng, F., Wang, F., Wang, J., Chiang, Y.-M., Jin, S. & Tang, M. (2017). *Nat. Commun.* **8**, 1194.
Kan, W. H., Deng, B., Xu, Y., Shukla, A. K., Bo, T., Zhang, S., Liu, J., Pianetta, P., Wang, B.-T., Liu, Y. & Chen, G. (2018). *Chem*, **4**, 2108–2123.
Li, S., Lee, S.-J., Wang, X., Yang, W., Huang, H., Swetz, D. S., Doriese, W. B., O'Neil, G. C., Ullom, J. N., Titus, C. J., Irwin, K. D., Lee, H.-K., Nordlund, D., Pianetta, P., Yu, C., Qiu, J., Yu, X., Yang, X.-Q., Hu, E., Lee, J.-S. & Liu, Y. (2019). *J. Am. Chem. Soc.* **141**, 12079–12086.
Li, S., Li, K., Zheng, J., Zhang, Q., Wei, B. & Lu, X. (2019). *J. Phys. Chem. Lett.* **10**, 7537–7546.
Lin, F., Liu, Y., Yu, X., Cheng, L., Singer, A., Shpyrko, O. G., Xin, H. L., Tamura, N., Tian, C., Weng, T.-C., Yang, X.-Q., Meng, Y. S., Nordlund, D., Yang, W. & Doeff, M. M. (2017). *Chem. Rev.* **117**, 13123–13186.
Lin, F., Markus, I. M., Nordlund, D., Weng, T.-C., Asta, M. D., Xin, H. L. & Doeff, M. M. (2014). *Nat. Commun.* **5**, 3529.
Lin, F., Nordlund, D., Li, Y., Quan, M. K., Cheng, L., Weng, T.-C., Liu, Y., Xin, H. L. & Doeff, M. M. (2016). *Nat. Energy*, **1**, 15004.
Liu, Y., Andrews, J. C., Wang, J., Meirer, F., Zhu, P., Wu, Z. & Pianetta, P. (2011). *Opt. Express*, **19**, 540–545.
Liu, Y., Meirer, F., Williams, P. A., Wang, J., Andrews, J. C. & Pianetta, P. (2012). *J. Synchrotron Rad.* **19**, 281–287.
Mao, Y., Wang, X., Xia, S., Zhang, K., Wei, C., Bak, S., Shadike, Z., Liu, X., Yang, Y., Xu, R., Pianetta, P., Ermon, S., Stavitski, E., Zhao, K., Xu, Z., Lin, F., Yang, X., Hu, E. & Liu, Y. (2019). *Adv. Funct. Mater.* **29**, 1900247.
Markevich, E., Salitra, G., Hartmann, P., Kulisch, J., Aurbach, D., Park, K.-J., Yoon, C. S. & Sun, Y.-K. (2019). *J. Electrochem. Soc.* **166**, A5265–A5274.
Meirer, F., Cabana, J., Liu, Y., Mehta, A., Andrews, J. C. & Pianetta, P. (2011). *J. Synchrotron Rad.* **18**, 773–781.
Mu, L., Yuan, Q., Tian, C., Wei, C., Zhang, K., Liu, J., Pianetta, P., Doeff, M. M., Liu, Y. & Lin, F. (2018). *Nat. Commun.* **9**, 2810.
Nelson Weker, J. & Toney, M. F. (2015). *Adv. Funct. Mater.* **25**, 1622–1637.
Nelson Weker, J., Wise, A. M., Lim, K., Shyam, B. & Toney, M. F. (2017). *Electrochim. Acta*, **247**, 977–982.
Singer, A., Zhang, M., Hy, S., Cela, D., Fang, C., Wynn, T. A., Qiu, B., Xia, Y., Liu, Z., Ulvestad, A., Hua, N., Wingert, J., Liu, H., Sprung, M., Zozulya, A. V., Maxey, E., Harder, R., Meng, Y. S. & Shpyrko, O. G. (2018). *Nat. Energy*, **3**, 641–647.
Steinrück, H.-G., Cao, C., Tsao, Y., Takacs, C. J., Konovalov, O., Vatamanu, J., Borodin, O. & Toney, M. F. (2018). *Energy Environ. Sci.* **11**, 594–602.
Tsai, E. H. R., Billaud, J., Sanchez, D. F., Ihli, J., Odstrčil, M., Holler, M., Grolimund, D., Villevieille, C. & Guizar-Sicairos, M. (2019). *iScience*, **11**, 356–365.
Wang, J., Karen Chen-Wiegart, Y., Eng, C., Shen, Q. & Wang, J. (2016). *Nat. Commun.* **7**, 12372.
Wang, M., Tan, Q. & Li, J. (2018). *Environ. Sci. Technol.* **52**, 13136–13143.
Wei, C., Xia, S., Huang, H., Mao, Y., Pianetta, P. & Liu, Y. (2018). *Acc. Chem. Res.* **51**, 2484–2492.
Wei, C., Zhang, Y., Lee, S.-J., Mu, L., Liu, J., Wang, C., Yang, Y., Doeff, M., Pianetta, P., Nordlund, D., Du, X.-W., Tian, Y., Zhao, K., Lee, J.-S., Lin, F. & Liu, Y. (2018). *J. Mater. Chem. A*, **6**, 23055–23061.
Xia, S., Mu, L., Xu, Z., Wang, J., Wei, C., Liu, L., Pianetta, P., Zhao, K., Yu, X., Lin, F. & Liu, Y. (2018). *Nano Energy*, **53**, 753–762.
Xu, J., Sun, M., Qiao, R., Renfrew, S. E., Ma, L., Wu, T., Hwang, S., Nordlund, D., Su, D., Amine, K., Lu, J., McCloskey, B. D., Yang, W. & Tong, W. (2018). *Nat. Commun.* **9**, 947.
Xu, R., Yang, Y., Yin, F., Liu, P., Cloetens, P., Liu, Y., Lin, F. & Zhao, K. (2019). *J. Mech. Phys. Solids*, **129**, 160–183.
Xu, Y., Hu, E., Zhang, K., Wang, X., Borzenets, V., Sun, Z., Pianetta, P., Yu, X., Liu, Y., Yang, X.-Q. & Li, H. (2017). *ACS Energy Lett.* **2**, 1240–1245.
Xu, Z., Rahman, M. M., Mu, L., Liu, Y. & Lin, F. (2018). *J. Mater. Chem. A*, **6**, 21859–21884.
Yan, P., Zheng, J., Chen, T., Luo, L., Jiang, Y., Wang, K., Sui, M., Zhang, J.-G., Zhang, S. & Wang, C. (2018). *Nat. Commun.* **9**, 2437.
Yan, P., Zheng, J., Gu, M., Xiao, J., Zhang, J.-G. & Wang, C.-M. (2017). *Nat. Commun.* **8**, 14101.
Yang, Y., Xu, R., Zhang, K., Lee, S., Mu, L., Liu, P., Waters, C. K., Spence, S., Xu, Z., Wei, C., Kautz, D. J., Yuan, Q., Dong, Y., Yu, Y., Xiao, X., Lee, H., Pianetta, P., Cloetens, P., Lee, J., Zhao, K., Lin, F. & Liu, Y. (2019). *Adv. Energy Mater.* **9**, 1900674.
Zhang, J., Li, Q., Ouyang, C., Yu, X., Ge, M., Huang, X., Hu, E., Ma, C., Li, S., Xiao, R., Yang, W., Chu, Y., Liu, Y., Yu, H., Yang, X.-Q., Huang, X., Chen, L. & Li, H. (2019). *Nat. Energy*, **4**, 594–603.
Zhang, K., Ren, F., Wang, X., Hu, E., Xu, Y., Yang, X.-Q., Li, H., Chen, L., Pianetta, P., Mehta, A., Yu, X. & Liu, Y. (2017). *Nano Lett.* **17**, 7782–7788.
Zhao, E., Zhang, M., Wang, X., Hu, E., Liu, J., Yu, X., Olguin, M., Wynn, T. A., Meng, Y. S., Page, K., Wang, F., Li, H., Yang, X.-Q., Huang, X. & Chen, L. (2019). *Energy Storage Mater.* **24**, 384–393.
Zhu, W., Liu, D., Paolella, A., Gagnon, C., Gariépy, V., Vijh, A. & Zaghib, K. (2018). *Front. Energy Res.* **6**, 66.